Supplementary Information for "Cooperative orbital moments and edge magnetoresistance in monolayer WTe_2"

Symmetry and WTe_2 low-energy Hamiltonian

The low-energy electronic excitations for monolayer WTe_2 can be described by a four-band Hamiltonian as $\mathcal{H} = \mathcal{H}_0 + \mathcal{H}_R + \mathcal{H}_I$ [22, 23]. Here $\mathcal{H}_0$ is the BHZ hamiltonian

$$\mathcal{H}_0(k_x, k_y) = \epsilon_{\mathbf{k}}\mathbb{I} + m_{\mathbf{k}} s_0 \boldsymbol{\tau}_z + v_x k_x s_z \tau_x - v_y k_y s_0 \tau_y \quad \text{(S1)}$$

where $\epsilon_{\mathbf{k}} = (\epsilon_c + \epsilon_v)/2$ is the dispersive part of the Hamiltonian and $m_{\mathbf{k}} = (\epsilon_c - \epsilon_v)/2$ is the momentum dependent mass capturing the topological inversion. Here, $\epsilon_i = c_{i,0} - c_{i,x}k_x^2 - c_{i,y}k_y^2$, $i \in \{c, v\}$ is the dispersion for conduction and valence band respectively. Taking $c_{c,0} = 1$ eV and $c_{v,0} = 0$ eV gives the magnitude of topological band inversion in Eq. (S1): $2M = 1$ eV [23]. Throughout the text we use values for $v_x = 1.71$ eVÅ and $v_y = 0.48$ eVÅ obtained from a model fitting with available ARPES data [11, 19]. We have chosen $(C_x, C_y) = (5.5, 4.5)$ eVÅ^2 parameter values used in the main text that are obtained by Löwdin partitioning [23] and lie in the typical range for C_x, C_y. Lastly, we note that since $\epsilon_{\mathbf{k}}\mathbb{I}$ is a scalar, contributing to spin/orbital blocks equally it does not affect the structure of the edge state wavefunctions. For brevity as well as clarity, below and in the main text, we have suppressed $\epsilon_{\mathbf{k}}$ dependence.

$\mathcal{H}_I$ and $\mathcal{H}_R$ capture Ising and Rashba SOC [22, 23] and can be written as

$$\mathcal{H}_R = -\delta_x s_x \tau_y, \quad \mathcal{H}_I = -\delta_z s_z \tau_y, \quad \text{(S2)}$$

where $\delta_{x(z)}$ is the Rashba (Ising) SOC strength. Here $\mathcal{H}_R$ couple the spin blocks, and $\mathcal{H}_I$ mix its spin texture. In the main text, and unless stated otherwise, we use parameter values for $\delta_z = 70$ meV and $\delta_x = 40$ meV. These are within the range of SOC strengths achievable in WTe_2 [22]. Together with H_0 above, the full hamiltonian at zero magnetic field is $\mathcal{H} = \mathcal{H}_0 + \mathcal{H}_R + \mathcal{H}_I$.

Emergent symmetries

We note that the low energy model $\mathcal{H}_0(k_x, k_y)$ in Eq. (S1) contains *emergent* symmetries $\mathcal{M}_x : x \to -x$ and $\mathcal{M}_z : z \to -z$, under which the Hamiltonian $\mathcal{H}_0(k_x, k_y)$ remains invariant. These emergent symmetries arise in the long wavelength description of monolayer WTe_2. Since they are spatial symmetries, they are valid even when TRS is broken.

Interestingly, the mirror operations $\mathcal{M}_x : x \to -x$ and $\mathcal{M}_z : z \to -z$ can be used to characterize the Ising and Rashba SOC in Eq. (S2). This means that $\mathcal{H}_{R(I)}$ vanishes when the system is symmetric under $\mathcal{M}_{z(x)}$. Therefore nonvanishing $\mathcal{H}_{R(I)}$ directly proceed broken $\mathcal{M}_{z(x)}$ and can be thought to arise from out-of-plane (in-plane) dipole moment. This is consistent with their microscopic origin as matrix elements of the relativistic spin-orbit interaction: $\hat{H}_{\rm so}(\mathbf{k}) \sim (\mathbf{k} + \hat{\mathbf{p}}/m_0) \cdot \mathbf{s} \times \nabla\phi(\mathbf{r})$ [25].

A similar analysis can also be applied for the QSH edge states in WTe_2. In the presence of an applied magnetic field, the QSH edge states along the x-edge can be generically described via Eq. (1) of the main text. Here we reproduce it for the convenience of the reader:

$$H^{\rm edge}(k_x) = \tilde{v}\sigma_z k_x + \frac{\mu_B}{2}\sum_{ij} g_{ij}\sigma_i B_j, \quad \text{(S3)}$$

where we have taken the lowest symmetry allowed terms, neglecting terms higher order in k and B. Note that the first term in Eq. (S3) is symmetric under both $\mathcal{M}_z$ and $\mathcal{M}_x$ operations.

We now concentrate on the second term of Eq. (S3). Under the mirror operation $\mathcal{M}_z$, we have

$$\begin{aligned} \sigma_{x,y} \to -\sigma_{x,y}, \quad \sigma_z \to \sigma_z, \\ B_{x,y} \to -B_{x,y}, \quad B_z \to B_z. \end{aligned} \quad \text{(S4)}$$

since $\boldsymbol{\sigma}$ and $\mathbf{B}$ are pseudo-vectors. This means that when the system is symmetric under $\mathcal{M}_z$, the out-of-plane B-field terms $g_{xz}\sigma_x B_z$ and $g_{yz}\sigma_y B_z$ must vanish.

We note that a further constraint can be gleaned by analyzing the behavior of Eq. (S3) under the mirror operation $\mathcal{M}_x$. In the same fashion as above, this operation flips $\mathbf{B}$ and $\boldsymbol{\sigma}$ perpendicular to x. This means that when the system is symmetric under $\mathcal{M}_x$, the B-field terms $g_{xz}\sigma_x B_z$, $g_{xy}\sigma_y B_x$, and $g_{yx}\sigma_x B_y$ must vanish. When both $\mathcal{M}_z$ and $\mathcal{M}_x$ are symmetries of the system, all off-diagonal terms in $g_{ij}\sigma_i B_j$ must vanish. Similarly, we note that while $g_{yz}\sigma_y B_z$ can manifest when $\mathcal{M}_z$ symmetry is broken but $\mathcal{M}_x$ symmetry is preserved. $g_{xz}\sigma_x B_z$ requires both $\mathcal{M}_x$ and $\mathcal{M}_z$ to be broken. This coincides with our analysis of COM in the main text that shows large g_{xz} arising when both $\delta_x, \delta_z \neq 0$.

Quantum Spin Hall edge states in WTe_2

The QSH edge states along an x-edge analyzed in the main text proceeds directly from the topological band inversion in Eq. (S1). In so doing we consider the following geometry: monolayer WTe_2 electrons occupy $y \geq 0$; $y < 0$ is the vacuum. The edge state spectrum and wavefunction spinor and spatial profile can be directly computed from $\mathcal{H}$ by setting $k_y \to -i\partial_y$ and solving for self-consistent wavefunction solutions. There are two principal methods to obtain the QSH edge states: (i) through an exact numerical solution (ENS) of the edge state spectrum by solving the coupled (in spin/orbital

space) Schrödinger equations and (ii) constructing the edge hamiltonian from the zero modes of $\mathcal{H}$. As shown in the main text, we perform both methods which display good agreement with each other. In this section, we describe both methods in more detail.

Exact numerical solution of edge state spectrum

We first describe the ENS method. The edge states at zero field can be obtained from an ENS of a set of coupled Schrödinger equations with $k_y \to -i\partial_y$ and appropriate boundary conditions. Including both the effect of orbital motion of electrons (through minimal coupling in the landau gauge $k_x \to k_x - eyB_z/\hbar c$) as well as a (spin) Zeeman effect found below in Eq.(S17) we write the coupled Schrödinger equations as

$$\left[\mathcal{H}\left(k_x - \frac{eyB_z}{\hbar c}, -i\partial_y\right) + \mathcal{H}_Z(\mathbf{B})\right]\boldsymbol{\xi}_{k_x}(y) = \epsilon\boldsymbol{\xi}_{k_x}(y) \tag{S5}$$

for each k_x along the x-edge. Here $\boldsymbol{\xi}(y) = \left[\xi_1(y), \xi_2(y), \xi_3(y), \xi_4(y)\right]^T$ is a general four component spinor wavefunction. Each of the $\xi_i(y)$ wavefunctions satisfy Dirichlet boundary conditions, $\xi_i(-L) = \xi_i(L) = 0$ on a strip geometry with $y \in [-L, L]$ and $L = 200$ nm. Here, as in the main text, $\mathbf{B} = |\mathbf{B}|(\sin\theta\cos\varphi, \sin\theta\cos\varphi, \cos\theta)$.

We solved Eq. (S5) numerically utilizing finite element analysis. The system of equations is solved along a line (along y-direction) of length $2L$ (composed of $2/10^{-3}$ elementary divisions) for every value of k_x to obtain the edge spectrum. Sample edge spectrum as a function of k_x along the x-edge are shown in Fig. S1 for various values of θ; here $\varphi = 0$.

In Fig. 1 and 3 of the main text we display gap size and edge resistance obtained from the ENS edge state spectrum as open circles. In obtaining the gap size at each orientation of magnetic field (θ, ϕ), we numerically obtained the minimum difference between upper (blue) and lower (red) bands in Fig. S1 to obtain the full size of the gap. Note the near gap closure in the edge spectrum for $\theta = 50°$ in Fig. S1 in agreement with the critical angle θ_c found in the main text.

Zero modes and constructing low-energy edge hamiltonian

In this section, we describe how to construct the low-energy edge hamiltonian from the zero modes of $\mathcal{H}(k_x, k_y \to -i\partial_y)$. Zero modes along the x-edge satisfy

$$\langle \mathbf{r}|\Psi\rangle = \sum_j a_j \exp(-y/\lambda_j)|u_j\rangle \exp[ik_x x] \tag{S6}$$

with the boundary condition $\Psi(y=0) = \Psi(y\to\infty) = 0$. Here λ_j is the decay length associated with j^{th} decay

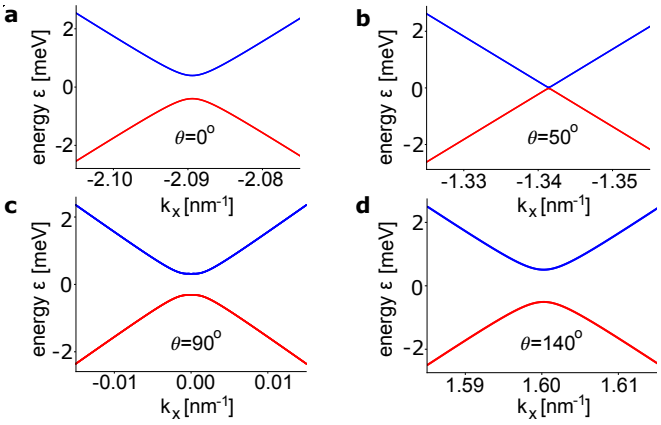

FIG. S1: (a,b,c,d) Edge spectrum generated from ENS algorithm (see text) by solving Eq. (S5) for magnetic field $\mathbf{B} = 7|(\sin\theta, 0, \cos\theta)$ T at $\theta = 0°, 50°, 90°, 140°$ respectively. Here, we use $\delta_x = 40$ meV and $\delta_x = 70$ meV for the strength of Rashba and Ising SOC respectively.

mode, $|u_j\rangle$ are 4 component spinors, and a_j is the corresponding normalization coefficients. The zero-mode spinors and decay constants satisfy $\mathcal{H}(0, \lambda_j^{-1})|u_j\rangle = 0$. Solving for the zeros of $\det[\mathcal{H}(0, \lambda_j^{-1})]$, we obtain zero-mode decay lengths

$$\lambda^{-1} = \pm\frac{v_y \pm \sqrt{v_y^2 - 4C_y(M \pm i\delta)}}{2C_y}, \quad \delta = \sqrt{\delta_x^2 + \delta_z^2} \tag{S7}$$

that can take on eight possible values. Using the boundary condition $\Psi(y \to \infty) = 0$, we discard four λ^{-1} in Eq. (S7) that have negative real parts (they are not normalizable in our space). The zero mode spinors that correspond to each λ_j can then be obtained numerically; using these we construct two degenerate zero modes. The edge hamiltonian (and the numerical edge state wavefunction) can then be obtained in the standard fashion by projecting the bulk hamiltonian $\mathcal{H}(k_x, 0)$ onto the space spanned by the degenerate zero modes in the same form as Eq. (1) of the main text. In our main text, these numerical edge state wavefunctions are employed in obtaining the orbital contributions to magnetoresponse (i.e. g_{xz} and g_{yz}) shown in Fig. 2 of the main text. (Spin) Zeeman contributions, see below, are similarly obtained using these same edge state wavefunctions. For clarity we denote these numerical edge eigenstates (NE).

While the above procedure is standard and can be implemented numerically, to gain further insight into the structure of the edge wavefunctions, we now analyze approximate zero-modes that that can be expressed in a simple closed form. As shown in the main text, these allow us to expose the origin of COM – cooperative spin canting. We do this by first noting that $\eta = v_y/(2\sqrt{MC_y}) = 0.15$ is small. Exploiting this small parameter, we expand λ^{-1} in Eq. (S7) in η and obtain

Eq. (7) of the main text

$$[\lambda_n^s]^{-1} = \frac{v_y}{2C_y} + \frac{n\delta}{2\sqrt{MC_y}} - ins\sqrt{\frac{M}{C_y}} + \sqrt{\frac{M}{C_y}}\mathcal{O}\left(\eta^2\right), \tag{S8}$$

where $\eta^2 = 0.02$ is small, and $s = \pm$ and $n = \pm$. In the same fashion as above, zero mode spinors can be obtained by solving the set of four simultaneous equations $\mathcal{H}(0, [\lambda_n^s]^{-1})|u_s\rangle = 0$, where $[\lambda_n^s]^{-1}$ is given by Eq. (S8). Using $M + C_y\,[\lambda_n^s]^{-2} = -2insM(\eta + n\Omega + \mathcal{O}(\eta^2, \Omega^2))$ and $v_y\,[\lambda_n^s]^{-1} = -2insM(\eta + \mathcal{O}(\eta^2, \eta\Omega))$, with $\Omega = \delta/(2M)$, the above system of equations yields the approximate zero-mode spinors in Eq. (6) of the main text:

$$|u_s\rangle = \mathcal{N}_s\left(\Sigma_s, \Sigma_s, 1, 1\right)^T, \quad \Sigma_s = (\delta_z + s\delta)/\delta_x, \tag{S9}$$

where $\mathcal{N}_+ = [2(\Sigma_s^2 + 1)]^{-1/2}$ and $\mathcal{N}_- = \mathrm{sgn}(\delta_x)[2(\Sigma_s^2 + 1)]^{-1/2}$. We note, parenthetically, that the choice of zero modes is not unique. Indeed, other linear combinations of zero modes shown above are equally valid and produce the same physical observables and dependencies (e.g., edge gap behavior as a function magnetic field).

Using Eq. (S8) and (S9), we can write approximate edge zero mode wave functions (see also Eq.(4) of the main text)

$$\langle \mathbf{r}|\Psi_s\rangle = \sum_n a_n^s \exp(-y/\lambda_n^s)|u_s\rangle, \tag{S10}$$

where we have identified the $s = \pm 1$ with the spin degree of freedom for the two fold degenerate edge modes and n represents the two-decay modes for each spin (note change in index j to n, s index). Next, we determine the coefficients a_n^s by using the other boundary condition $\Psi(y = 0) = 0$, according to which $\sum a_n^s|u_s\rangle = 0$ is satisfied by $a_n^s = \{1, -1\}$. This leads to the degenerate edge wavefunctions $|\Psi_s\rangle = \mathcal{K}\left[\exp\left(-y/\lambda_+^s\right) - \exp\left(-y/\lambda_-^s\right)\right]|u_s\rangle$ with normalization constant $\mathcal{K} = \left[(v_y^2 M - \delta^2 C_y)/(2v_y M C_y)\right]^{1/2}$.

The edge Hamiltonian can be obtained by projecting $\mathcal{H}_0(k_x, 0)$ onto the zero modes in Eq. (S10) by computing the matrix elements $\langle\Psi_\mu|\mathcal{H}_0(k_x, 0)|\Psi_\nu\rangle$, with $\mu, \nu \in s$ producing:

$$H(k_x) = v_x k_x\left(\gamma\sigma_z + \mathbf{Re}[\Gamma]\sigma_x + \mathbf{Im}[\Gamma]\sigma_y\right), \tag{S11}$$

where $\tan\chi_1 = \mathrm{sgn}(\delta_x)|\Gamma|/\gamma$ and $\tan\chi_2 = \mathrm{Im}[\Gamma]/\mathrm{Re}[\Gamma]$ where $\mathrm{Re}[\Gamma] = \delta_x[1/(\delta) - \delta C_y/(v_y^2 M)]$ and $\mathrm{Im}[\Gamma] = \delta_x[(v_y^2 M - \delta^2 C_y)/(4M^3 C_y)]$ is controlled by the Rashba coupling, and $\gamma = \delta_z/\delta$ is controlled by the Ising coupling.

Eq. (S11) can can be diagonalized by the unitary operation $\mathcal{P}^{-1} H \mathcal{P} = \tilde{v} k_x \sigma_z$ producing the first term in Eq. (1) of the main text. Here we have used

$$\mathcal{P} = \begin{pmatrix} \cos\frac{\chi_1}{2} e^{i\chi_2/2} & \sin\frac{\chi_1}{2} e^{i\chi_2/2} \\ \sin\frac{\chi_1}{2} e^{-i\chi_2/2} & -\cos\frac{\chi_1}{2} e^{-i\chi_2/2} \end{pmatrix} \tag{S12}$$

Further, the corresponding edgestate eigenfunctions can be similarly written as $(|\Phi_1\rangle, |\Phi_2\rangle)^T = \mathcal{P}^{-1}\left(|\Psi_+\rangle, |\Psi_-\rangle\right)^T$, see also Eq. (5) of the main text.

Magnetic field induced gap opening

In this section, we discuss how magnetic field opens up a gap in the edge spectrum by analyzing how both (i) the orbital motion of electrons, and (ii) a (spin) Zeeman interaction, can affect the structure of the edge eigenstates.

Orbital magnetoresponse

COM discussed in the main text can be directly obtained from analyzing the behavior of the edge eigenstates, characterized by Eq. (5) in the main text, when orbital motion of electrons is included. The orbital motion of an electron in an external magnetic field is described by minimal coupling $\mathcal{H}(\mathbf{k} - e\mathbf{A}/(\hbar c))$, where we have used a Landau gauge $\mathbf{A} = (yB_z, 0, 0)$ for the electron along x-edge. The orbital motion produces B_z dependent terms in Eq. (1) that go as $H_{mn}^{\mathrm{orb}} = \langle\Phi_m|\mathcal{H}_0(-eyB_z/(\hbar c), 0)|\Phi_n\rangle$, with $m, n \in \{1, 2\}$ index the spin-orbit mixed edge eigenstates in Eq. (5) of the main text. Orbital motion only arises for a perpendicular field, vanishing for in-plane fields.

We note that terms that go as σ_z commute with the first term of Eq. (1) of the main text, and hence cannot gap out the edge states; instead they shift the position of the gapless Dirac point in momentum space. As a result, we focus only on the off diagonal elements $H_{12}^{\mathrm{orb}} = H_{21}^{\mathrm{orb}*}$ which can gap the spectrum. As discussed in the main text, we use the numerical edge eigenstates NE method to H^{orb}. Comparing with Eq. (1) we plot the gyromagnetic coefficients g_{xz} and g_{yz} shown in Fig. (2) of the main text.

The same analysis can be performed using the approximate edge eigenstates that proceed from Eq. (S12). Using these approximate edge eigenstates we find

$$\begin{aligned} H_{12}^{\mathrm{orb}} \approx{}& \cos\frac{\chi_1}{2}\sin\frac{\chi_1}{2}\left(\mathcal{M}_{++} - \mathcal{M}_{--}\right) \\ &+ \sin^2\frac{\chi_1}{2} e^{-i\chi_2}\mathcal{M}_{-+} - \cos^2\frac{\chi_1}{2} e^{i\chi_2}\mathcal{M}_{+-} \end{aligned} \tag{S13}$$

where $\mathcal{M}_{ij} = \langle\Psi_i|\mathcal{H}_0(-eyB_z/(\hbar c), 0)|\Psi_j\rangle$ matrix elements composed of the initial zero modes $i, j \in s$. Writing out $\mathcal{M}_{ij}$ dependence on WTe_2 parameters gives

$$\begin{aligned} &\cos\frac{\chi_1}{2}\sin\frac{\chi_1}{2}\left(\mathcal{M}_{++} - \mathcal{M}_{--}\right) \\ &\quad\approx -\frac{ev_x\delta_z\delta_x}{\hbar c\delta^2}\mathcal{K}^2\left[\frac{2C_y^2(v_y^2 M + \delta^2 C_y)}{v_y^2(v_y^2 M - \delta^2 C_y)}\right]B_z \end{aligned} \tag{S14}$$

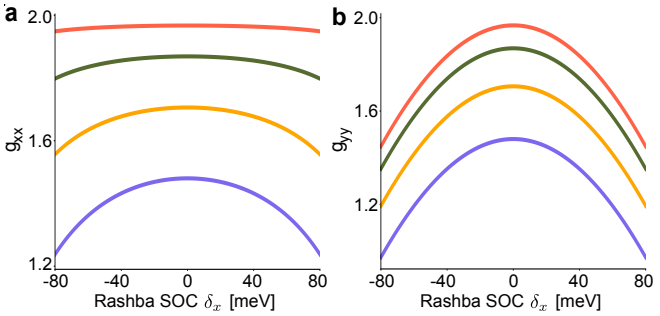

FIG. S2: Variation of g_{xx} (panel a.) and g_{yy} (panel b.) with Rashba SOC at different magnitude of Ising SOC (top to bottom: 20, 40, 60, 80 meV).

and

$$\sin^2\frac{\chi_1}{2}e^{-i\chi_2}\mathcal{M}_{-+}-\cos^2\frac{\chi_1}{2}e^{i\chi_2}\mathcal{M}_{+-} \approx \frac{ev_x}{\hbar c}\mathcal{K}^2\left[\frac{2C_y^2\delta_x\delta_z}{v_y^2\delta^2}+i\frac{C_y\delta_x}{2M^2}\right]B_z \quad \text{(S15)}$$

valid in the small η and small Ω limit. Plugging into Eq. (S13) produces an approximate $H_{12}^{\rm orb}$. Finally, comparing with $\mu_B gB/2$, the real part of $H_{12}^{\rm orb}$ gives g_{xz} and the (negative) imaginary part yields g_{yz} as

$$g_{xz}\approx-\frac{8m_e v_x C_y^2\delta_x\delta_z}{\hbar^2 v_y^3 M}+\mathcal{O}(\eta^2),\quad g_{yz}\approx-\frac{m_e v_x v_y\delta_x}{\hbar^2 M^2}, \quad \text{(S16)}$$

As discussed in the main text, g_{xz} requires both $\delta_x,\delta_z\neq 0$ manifesting a *cooperative* effect of COM – this yields sizable spin canting and a significant COM of several Bohr magnetons. In contrast, g_{yz} only requires $\delta_x\neq 0$ but is suppressed taking on values of $g_{yz}\sim 0.02$ that is suppressed by a large M. Here we have used the same WTe_2 parameters as the main text.

Spin Zeeman magnetoresponse

We now turn to the *spin* Zeeman interaction, wherein the magnetic field directly couples with the *spin moments* of the electrons. This starkly contrasts with the *orbital* effect of COM which we focussed on in the main text. Following the projection procedure described above, the Zeeman effect on the edge can be obtained by projecting bulk spin Zeeman interactions on the edge eigenstates as $[H_Z^{\rm edge}]_{mn}=\langle\Phi_m|\mathcal{H}_Z(\mathbf{B})|\Phi_n\rangle$, $m,n\in\{1,2\}$ where

$$\mathcal{H}_Z(\mathbf{B})=\frac{\mu_B}{2}\left[s_zB_z\left(\mathcal{G}_\perp^+\tau_0+\mathcal{G}_\perp^-\tau_z\right)+(s_xB_x+s_yB_y)\left(\mathcal{G}_{||}^+\tau_0+\mathcal{G}_{||}^-\tau_z\right)\right] \quad \text{(S17)}$$

where $\mathcal{G}_{\perp,||}^{\pm}=\left(g_{\perp,||}^e\pm g_{\perp,||}^h\right)/2$ with $g_{\perp,||}^{e,h}$ being the bulk gyromagnetic coefficients for electron/holes in response to out-of-plane/in-plane magnetic field. In our plots, we use bulk Lande g-factors of order 2, so that $\mathcal{G}_{||}^+=2$. Other values of g can be used as well, and do not qualitatively affect our results

Using Eq.(S17) we plot the effective (in-plane) gyromagnetic coefficients g_{xx} and g_{yy} for the edge electrons are shown in Fig. S2. In so doing we have used the numerical edge eigenstates using the NE method. Rashba and Ising couplings can renormalize these coefficients so that $\max(g_{xx},g_{yy})=\mathcal{G}_{||}^+$ when $\delta_x,\delta_z=0$. In the range of Rashba and Ising SOC we consider, these produce $g_{xx},g_{yy}\sim 1.2-2$

We note that when magnetic field is applied in the z-direction, the (spin) Zeeman interaction does not open a gap in the edge spectrum as discussed in Ref. [12–14]. Instead, it shifts spectrum in momentum space. This directly proceeds from $[\mathcal{H}_0(k_x,0),\mathcal{H}_Z(B_z)]=0$ as can be readily verified from Eq. (S17). Here $\mathcal{H}_0(k_x,0)$ is the dispersing part of bulk hamiltonian that produces the gapless first term of Eq. (1) of the main text (i.e. the QSH gapless edgestates at $B=0$). Projecting on the edge yields $[H^{\rm edge}(\mathbf{B}=0),H_Z^{\rm edge}(B_z)]=0$ for any choice of spinor basis. As a result, the (spin) Zeeman interaction along the edge does not open a gap in the edge spectrum when $\mathbf{B}=B_z\hat{\mathbf{z}}$.

Including both the orbital and (spin) Zeeman contributions we obtain the variation of (full) gap size with orientation of magnetic field, see Fig. 1 of the main text, as

$$\Delta=\mu_B|\mathbf{B}|\left[(g_{xx}\cos\varphi\sin\theta+g_{xz}\cos\theta)^2+(g_{yy}\sin\varphi\sin\theta+g_{yz}\cos\theta)^2\right]^{1/2}. \quad \text{(S18)}$$

Specializing to $\varphi=0$ and noting that $g_{yz}\ll g_{xz},g_{xx}$ produces Eq. (9) of the main text.

Edge states along other edge orientations

In the main text we focused on the behavior of COM and edge states along the x-edge. However, we note that edge termination as well as orientation can also influence edge behavior as detailed in Ref. [28, 29]. For instance, the extent of the edge state wavefunction can change depending on the edge termination [29].

A full discussion of the sensitivity of edge behavior to edge termination and orientation is beyond the current scope of our work. Nevertheless, in this section we provide a simple illustrative demonstration of a different edge orientation. This can be done by fixing the mirror axis in absolute space (i.e. parallel to x-edge), and considering an edge at an angle to the x-edge (see Fig. S3a). To track the electrons along this Θ-edge, we use new momenta $\mathbf{k}'=(k'_x,k'_y)$, where k'_x is parallel to the Θ-edge and k'_y is perpendicular to the Θ-edge. Using these new

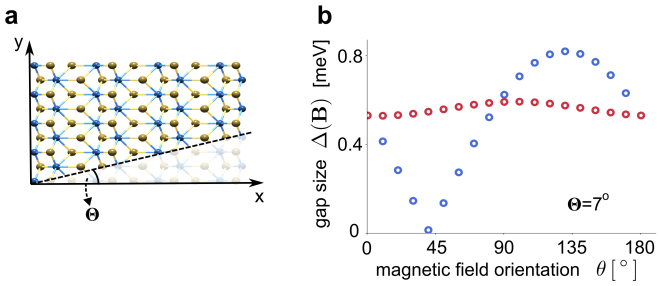

FIG. S3: (a) Illustration of an edge at an angle Θ from the x-edge so that the electron momenta between two edges are related by Eq. (S19). (b) Gap size (calculated using ENS method, see above) for an edge oriented at $\Theta = 7^\circ$ from the x-edge. (Blue circles) Magnetic field is applied $x-z$ plane ($\phi = 0$) plane; (Red circles) Magnetic field is applied in the $y-z$ plane. We have used $|\mathbf{B}| = 7$ T with $\delta_x = 40$ meV and $\delta_z = 70$ meV for Rashba and Ising SOC strength respectively. Here we have additionally chosen $\mathcal{G}_\parallel^- = 0.05$ as an illustration.

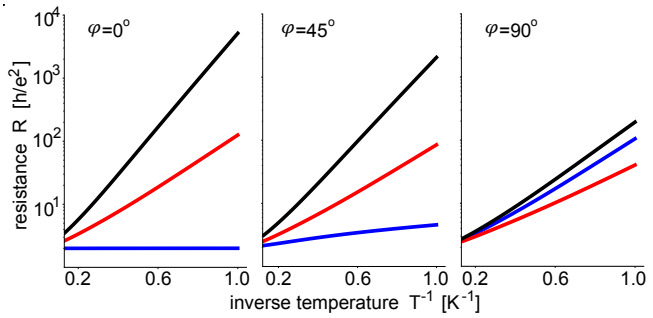

FIG. S4: Temperature variation of resistance at different orientations of magnetic field shown at $\theta = 50$ (blue), 95 (red), 140 (black) for $\varphi = 0, 45^\circ$ and 90°. Anisotropic trends are seen for $\varphi = 0$ which subside as the azimuthal is changed from 0 to 90°. Here, $|\mathbf{B}| = 7$ T with chemical potential fixed at $\mu = 0.3$ meV.

momenta we can express the Hamiltonian in Eq. S5 in terms of the new momenta by writing

$$\begin{pmatrix} k_x \\ k_y \end{pmatrix} = \begin{pmatrix} \cos\Theta & \sin\Theta \\ -\sin\Theta & \cos\Theta \end{pmatrix} \begin{pmatrix} k'_x \\ k'_y \end{pmatrix} \tag{S19}$$

and Θ is the angle between orientation of new edge and x-edge. We calculate the edge state spectrum using the ENS scheme as described above with the same Dirichilet boundary conditions applied instead now on the Θ-edge.

The corresponding gap in the edge spectrum in the presence of magnetic field can be similarly obtained directly using ENS (see Fig. S3), where we substitute $k'_y \to -i\partial_{y'}$ and $k'_x \to (k'_x - ey'B/(\hbar c))$ as before. As a demonstration we show the edge gap opening for $\Theta = 7^\circ$ demonstrating that the large gap opening from an orbital contribution persists in Fig. S3. In Fig. S3, we find that maximal achievable gaps have now decreased, and $\Delta(\mathbf{B})$ as a function of magnetic field orientation in the $y-z$ plane (red circles) is different from that expected when the edge was along x alone. Nevertheless, COM magnetic moments (evidenced by pronounced gaps when a perpendicular magnetic field is applied) persist.

Numerical edge resistance at various φ and T

The gap opening in the edge state spectrum $\Delta(\mathbf{B})$ when magnetic field is applied directly impacts edge transport producing an edge magnetoresistance. We track the resistance along the edge via $R(\mathbf{B}) = R_c + R_s(\mathbf{B})$, where R_c is the contact resistance while R_s is the resistance of edge channel. The latter can be computed via $R_s(\mathbf{B}) = L\rho(\mathbf{B})$, where L is the length of the channel and $\rho(\mathbf{B})$ is the resistivity of the edge channel [30, 31]: $[\rho(\mathbf{B})]^{-1} = e^2 \sum_{k_x} (\partial\varepsilon/\hbar\partial k_x)^2 \tau(\varepsilon)(-\partial_\varepsilon f)$ where $\varepsilon(k_x)$ are the eignenergies of Eq. (1), $f = \{1 + \exp[\beta(\varepsilon - \mu)]\}^{-1}$ is the Fermi function and $[\tau(\varepsilon)]^{-1} = (2\pi/\hbar)\nu(\varepsilon)|\langle\psi(-k_x)|V(x)|\psi(k_x)\rangle|^2$ is the relaxation rate. Here $\psi(k_x)$ are the eigenstates of Eq. (1), $\nu(\varepsilon)$ the density of states of the 1D edge channel, μ the chemical potential, $\beta = 1/k_BT$, and $V(x)$ is the impurity potential. In what follows, we choose short range impurities $V(x) = \sum_j u\delta(x - x_j)$ as an illustration with u the strength of a single impurity and j sums over all impurities in the channel. The disorder average $\langle V(x)V(x')\rangle = n_{\rm imp}u^2\delta(x - x')$, where $n_{\rm imp}$ is the impurity density yielding a length scale $\ell_0 = \tilde{v}^2/(\mathcal{U}^2 n_{\rm imp})$ [32, 33]. We note that the mean free path of a 1D electron system with left and right movers can be written as $\ell = \ell_0/|\langle\psi(-k_x)|\psi(k_x)\rangle|^2$. For a helical 1D liquid at $\mathbf{B} = 0$, ℓ diverges since the left- and right-movers are time-reversed pairs yielding $\langle\psi(-k_x)|\psi(k_x)\rangle$ that vanishes. However, when $\mathbf{B} \neq 0$, this protection is lifted, and $\langle\psi(-k_x)|\psi(k_x)\rangle \neq 0$ allowing finite mean free-paths. For completely non-helical liquids $\langle\psi(-k_x)|\psi(k_x)\rangle = 1$ yielding $\ell = \ell_0$ as expected for the "non-helical" mean free path. In all plots of resistance in the main text and the supplement we have usede used device parameters $L = 500\,$nm, $\ell_0 = 100\,$nm, $R_c = h/2e^2$ and a chemical potential fixed at $\mu = 0.3\,$meV as an illustration.

We also investigate the temperature dependence of resistance for various azimuthal angles and we find anisotropic (magnetoresistance) temperature dependence of resistance at is most pronounced for $\varphi = 0$. As the gap almost closes at $\mathbf{B}_*$, for any finite chemical potential, there are free carriers in the conduction band and we see a minimum resistance at $\theta = \theta_c$, that is insensitive to temperature (panel a in Fig. S4, blue curve). In contrast, as we change the azimuthal angle from 0 to 90°, the gap size at $\theta = \theta_c(90 + \theta_c)$ increases (decreases) significantly, and the minima (maxima) in gap shifts towards 90° (0°). This reduces the anisotropy in the temperature variation in resistance, which is most evident at $\varphi = 0$, see Fig. S4. In plotting the resistance in Fig. S4 we have

used the same parameters as the main text.